ISSN 1349-1113
JAXA-RR-05-030E

JAXA Research and Development Report

Comparative Force/Heat Flux Measurements between JAXA Hypersonic Test Facilities Using Standard Model HB-2 (Part 2: High Enthalpy Shock Tunnel Results)

Shigeru KUCHI-ISHI, Shigeya WATANABE,
Schuichi UEDA, Hideyuki TANNO, Tomoyuki KOMURO,
Kazuo SATO, and Katsuhiro ITOH

March 2006

Japan Aerospace Exploration Agency

Comparative Force/Heat Flux Measurements between JAXA Hypersonic Test Facilities Using Standard Model HB-2 (Part 2: High Enthalpy Shock Tunnel Results)

Shigeru KUCHI-ISHI[*1], Shigeya WATANABE[*1],
Schuichi UEDA[*2], Hideyuki TANNO[*2], Tomoyuki KOMURO[*2],
Kazuo SATO[*2], and Katsuhiro ITOH[*2]

口石　茂[*1]、渡辺重哉[*1]、植田修一[*2]、丹野英幸[*2]
小室智幸[*2]、佐藤和雄[*2]、伊藤勝宏[*2]

ABSTRACT

This report presents a detailed description and results of force and heat flux measurements conducted at the High-Enthalpy Shock Tunnel (HIEST) of the Japan Aerospace Exploration Agency (JAXA). The HB-2 standard hypersonic ballistic configuration was employed as a model. The force measurement tests used an aluminium alloy model and a three-component aerodynamic balance. An acceleration compensation technique was used to remove vibration components from the original data. Heat flux measurement tests used a chromel model with a total of 28 co-axial thermocouples press-fitted onto the surface. Time histories of temperature data were numerically integrated to determine the surface heat flux by applying one-dimensional heat conduction theory. Both force and heat tests used a conical nozzle, and a total of three enthalpy levels of 4, 8, and 11 MJ/kg and two levels of 4 and 8 MJ/kg were set for the force and heat tests, respectively. Although much higher stagnation enthalpy can be attained, relatively lower enthalpy levels were selected to compare with a blow-down type hypersonic wind tunnel and to alleviate uncertainties inherent in high-enthalpy facilities. The force test results correlated well with other hypersonic wind-tunnel data for the axial force coefficient at the enthalpy level of 4 MJ/kg, while a notable discrepancy was observed at the higher enthalpy levels of 8 and 11 MJ/kg. The real gas effects on aerodynamic characteristics are examined and discussed. In the heat test, a comparison of the heat flux distribution along the surface with data obtained in a blow-down type hypersonic wind tunnel showed good agreement in the nose part, typically within several percent. The present experiment was conducted as a series of comparative test campaigns between two hypersonic facilities in JAXA. Since the tunnel stagnation conditions and the corresponding data are tabulated in detail for each shot, the present test data are believed to serve as a complete database for evaluating aerodynamic force and heat flux data obtained at large-scale high-enthalpy shock tunnels.

Keywords: high-enthalpy shock tunnel, standard model, aerodynamic force, heat flux

概　　要

本報告は、JAXA高エンタルピ衝撃風洞（HIEST）において実施された、HB-2形状バリスティック標準模型を用いた空気力/空力加熱率測定試験結果に関するものである。力試験はアルミ製模型に十字一列型3分力天秤を装着して実施され、データの振動成分を除去するために加速度補正が施された。熱試験で用いられた模型はクロメル製で計28個の同軸熱電対が装着されてあり、温度時間履歴データを1次元熱伝導の仮定の下で数値的に積分することにより加熱率を求めた。力/熱試験共にコニカルノズルを使用し、力試験については

＊1　Wind Tunnel Technology Center, Institute of Aerospace Techology（総合技術研究本部風洞技術開発センター）
＊2　Kakuda Space Center, Institute of Aerospace Technology（総合技術研究本部角田宇宙センター）

エンタルピ4, 8, 11 MJ/kg、熱試験については4, 8 MJ/kgの試験条件でそれぞれ実施された。力試験結果はエンタルピ4 MJ/kg条件の場合、軸力係数に関して他風洞の試験データと良好な傾向の一致を示している一方で、8, 11 MJ/kgの場合は系統的なずれが観測されており、実在気体効果の影響が可能性として示唆される。一方熱試験における無次元加熱率データは、ブローダウン式コールド極超音速風洞データと模型頭部において数%程度の範囲でよい一致を示した。本試験は、JAXA極超音速関連風洞対応風試の一環として実施されたものであり、また本試験データは高エンタルピ衝撃風洞における基礎データとしても有用である。

NOMENCLATURE

A = Reference area, $\pi D^2/4$
a = Acceleration
A_b = Model base area
C_A = Zero-lift gross (total) axial force coefficient, $F_x/q_\infty A$
C_{AF} = Zero-lift forebody axial force coefficient, $C_A-(p_\infty-p_bA_b)/A$
C_∞ = Chapman-Ruebesin constant
c = Specific heat
D = Reference centerbody diameter (see Fig. 2)
F_x = Axial aerodynamic force measured by the balance
H = Enthalpy per unit mass
k = Thermal conductivity, main coefficient of balance
M = Mach number
m = Equivalent inertia mass
P_{pit} = Pitot pressure
P_0 = Tunnel stagnation pressure
p = Static pressure
p_b = Base pressure
q = Heat flux, dynamic pressure
R = Gas constant
Re = Free-stream Reynolds number based on centerbody diameter
R_n = Nose radius of hemisphere
T = Temperature
T_0 = Tunnel stagnation temperature
t = Time
u = Velocity
V_{sh} = Shock speed at the shock tube end
$\bar{v}$ = Viscous interaction parameter, $M\sqrt{C_\infty/\mathrm{Re}}$
x = Balance voltage output, axial distance
μ = Viscosity coefficient
ρ = Density

Subscripts

stg = Stagnation
w = Model surface (wall)
0 = Stagnation, initial
∞ = Free-stream

1. INTRODUCTION

In designing and developing future hypersonic flight vehicles, accurate prediction of aero-thermal characteristics during the atmospheric re-entry is of particular importance. Due to limitations of conventional ground-based experimental facilities, it is practically impossible to produce flows of desired Mach number, Reynolds number, and total enthalpy which exactly match actual flight conditions. A numerical prediction obtained by applying computational fluid dynamic (CFD) techniques is to date insufficient in terms of reliability since it includes a number of uncertainties for both the numerical and physical aspects. Therefore, it is apparent that the use of either an experimental or numerical approach alone is inadequate for a reliable flight prediction and applying all of the possible approaches in determining the prediction is the best method for obtaining high accuracy from a general point of view.

The Japan Aerospace Exploration Agency (JAXA) has two large-scale hypersonic facilities called the 1.27 m Hypersonic Wind Tunnel (HWT) and High Enthalpy Shock Tunnel (HIEST). These facilities are common in the sense that they cover hypersonic speeds, but there are a number of differences regarding the free stream properties and tunnel specifications. Specifically, HWT is a blowdown type wind tunnel and therefore its flow properties can be calibrated well and the flow duration time is sufficiently long to measure accurate data. However, the stagnation enthalpy attainable in HWT is approximately 1 MJ/kg and is much lower than actual flight conditions at hypersonic speeds. On the contrary, in HIEST, although much higher enthalpy levels up to 25 MJ/kg can be obtained, there are many unknown factors inherent to the high-enthalpy short duration facilities. Hence it is meaningful to use these facilities in a synergistic way, such that the merits of one facility compensates for demerits in the other and vice versa. In other words, one facility should be used to improve capability and/or accuracy of the other such that both facilities benefit.

From this viewpoint, in JAXA, a comparative test program was initiated and performed for the above two facilities to obtain force/heat flux data using a common model configuration. Our

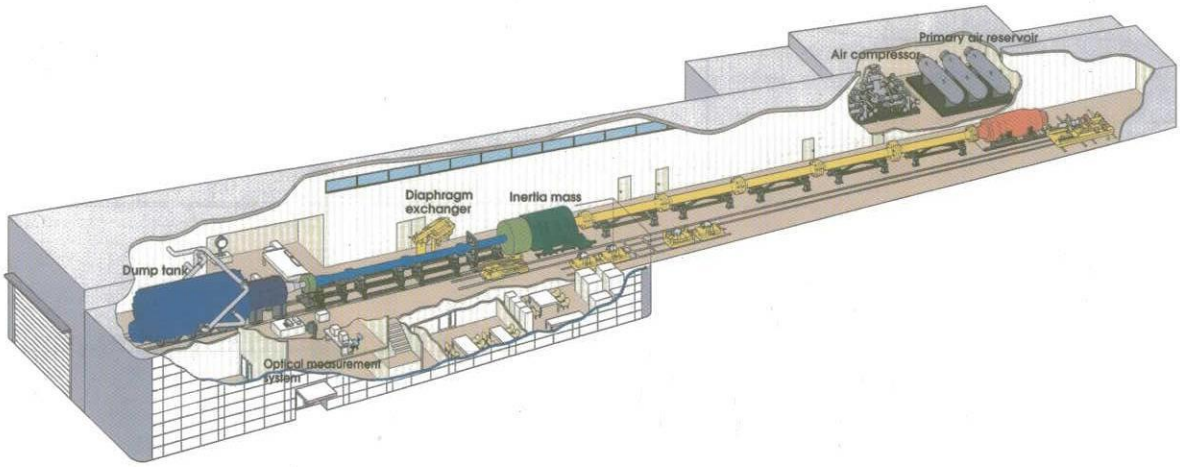

Fig. 1 JAXA High Enthalpy Shock Tunnel (HIEST).

final goal is to have a practical guideline for accurately and reliably predicting aero-thermodynamic properties of actual flight vehicles through the synergistic use of these facilities together with the aid of CFD. Of the two, the force and heat flux measurement tests conducted in HWT were already reported in detail in Ref. [1].

In the present report, results are presented for the HIEST force/heat flux tests performed as a succeeding part of the comparative test campaign using a ballistic-type model configuration designated as HB-2. The tests were conducted at three nominal enthalpy levels of 4, 8, and 11 MJ/kg for the force tests and two levels of 4 and 8 MJ/kg for the heat tests, respectively. Both for the force and heat tests, the data are compared with existing experimental results obtained at other hypersonic facilities including the HWT data and accuracy of the present data are examined. Since the experimental data and corresponding tunnel stagnation conditions are presented in detail, this report is believed to be one of the first publishment which includes a set of detailed force/heat flux data obtained in a large high-enthalpy shock tunnel and useful as a database for the validation of hypersonic CFD codes.

2. FACILITY

A schematic view of HIEST is shown in Fig. 1. HIEST is a large-scale free-piston type shock tunnel which consists of a high pressure air reservoir, compression tube, shock tube, nozzle, test section, and dump tank. The total length and weight of the facility is approximately 80 m and 300 tons, respectively.

The basic operation procedure of this facility is as follows. The high-pressure air in the secondary air reservoir (20 MPa maximum) launches a piston into the compression tube filled with helium as a driver gas at an initial pressure of 100 kPa. The piston is accelerated up to 400 m/sec and the driver gas is adiabatically compressed in the compression tube. At the end of the compression tube, a high-pressure diaphragm, which separates the compression tube and shock tube, ruptures at a certain pressure. This results in generating a strong shock wave inside the shock tube, so that a high-enthalpy stagnation condition of the test gas can be attained behind the reflected shock wave at the shock tube end. Furthermore, the shock tube and nozzle is separated with a thin plastic diaphragm, which easily ruptures when the shock wave arrives. The high-pressure, high-temperature test gas expands through the nozzle throat made of copper alloy.

The Mach number and unit Reynolds number in this facility range from 6 to 10 and 2.5×10^5 to 1.0×10^7 /m, respectively. A conical nozzle with exit diameter of 1.2 m and half-apex angle of 12 degree is utilized. The nozzle throat diameter is exchangeable to obtain various free stream Mach numbers and Reynolds numbers.

A more detailed description of the facility is found in Ref. [2].

3. MODELS

3.1 Model configuration

In the present study, a relatively simple model configuration was employed because it is preferable to minimize uncertainties coming from any geometrical complexity from the viewpoint of tunnel-to-tunnel comparison. The HB-2 type model employed in the present test is a standard model proposed in a joint program of the Advisory Group for Aerospace Research and Development (AGARD) and Supersonic Tunnel Association (STA) in 1950-60's [3]. This has an analytical shape that consists of a sphere, cone, cylinder, and flare as shown in Fig. 2.

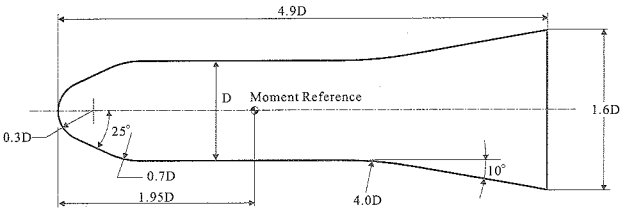

Fig. 2 HB-2 configurations.

Table 1 Nominal test conditions

Condition	A	B	C	D	E
Throat diameter (mm)	40	40	40	50	40
H_0 (MJ/kg)	4	8	8	8	11
P_0 (MPa)	15	20	45	45	30
M	9.9	8.5	8.1	7.6	7.8
Re ($\times 10^6$ 1/m)	0.9	0.4	0.8	1.2	0.5

3.2 Force model and three-component aerodynamic balance

The force model used in the present study is made of aluminium alloy (A7075) and the weight is 4.78 kg without the balance. The length and centerbody diameter of the model are 490 mm and 100 mm, respectively. The nose part is exchangeable with an alternative part which has a screw hole in the head to allow dynamic calibration tests using a fracture stick. The three-component aerodynamic balance installed in the model has an integral structure with the sting-model support system. A cross-beam type balance having high stiffness was used to enhance the response speed in the axial direction. The capacity of the balance with respect to the axial force, normal force, and the pitching moment are 980 N, 4,900 N, and 147 Nm, respectively. The main coefficients obtained from a static calibration test are 11,793 N/mV, 10,803 N/mV, and 47.523 Nm/mV corresponding to the axial force, normal force, and pitching moment.

To reconstruct axial force from the output signal containing vibrational effects, the acceleration compensation was made by using two accelerometers (ENDEVCO 2250A-10) attached to an adapter in front of the balance. The sensitivity of the accelerometer is 10.22 mV/G. A detailed schematic of the model is illustrated in Fig. A1 of Appendix A.

3.3 Heat model

A common heat model between the HIEST and HWT was fabricated and used in the present test campaign since the dimension of the test section of these facilities are almost identical. The length and centerbody diameter of the model are 490 mm and 100 mm, the same as the force model. In this model, a total of 28 chromel-constantan type co-axial thermocouples of 1.5 mm diameter (Medtherm TCS-E-10370) were press-fitted. A total of 8 sensors circumferentially located in the flare part were used in the HWT test as a check on the symmetry of the measurements. The model is made of chromel in order to avoid electromotive force caused by the difference of thermoelectric properties between the material of the model surface and the outer tube of the thermocouple [4]. The position of each sensor is illustrated in Fig. A2 and tabulated in Table A1 of Appendix A.

4. EXPERIMENTAL PROCEDURE

4.1 Test conditions

The detail of the present test conditions is as follows. A conical nozzle with an exit diameter of 1.2 m and a half-apex angle of 12 degree was utilized. Concerning the nozzle throat diameter, two different sizes of 40 mm and 50 mm were used to obtain various free stream Mach numbers and Reynolds numbers for the force tests, whereas it was fixed to 50 mm for the heat tests. The nominal test conditions of the present force/heat tests are summarized in Table 1. The reservoir pressure was measured by two pressure sensors placed at the shock tube end and the reservoir enthalpy was determined from the measured shock speed and the reservoir pressure assuming equilibrium chemical compositions. The free stream conditions were then computed using the one-dimensional nozzle flow program NENZF [5] with the reservoir conditions as input.

Although much higher stagnation enthalpies can be attained, relatively lower enthalpy levels were chosen in the present study (such low enthalpy conditions can be realized by increasing the mass fraction of argon gas in the driver tube). This is based on the concept that an emphasis is placed on the assessment of the measurement data obtained at a short duration facility by comparing with a blow-down type cold wind tunnel whose flow properties are expected to contain less uncertainties. In this sense, it is preferable to minimize uncertainties inherent to a high enthalpy facility such as nozzle throat erosion and flow contamination. At each enthalpy level, repeat shots were made to examine data repeatability. Both for force and heat tests, the angle of attack was fixed to zero degrees and the model was installed on the nozzle center axis.

Photographs of the heat model/support system, overview of the nozzle/test section, and the model placed in the test section are provided in Figs. 3, 4, and 5, respectively. Two permanent probes which have a hemispherical nose with a radius of 10 mm and monitor the Pitot pressure and the stagnation point heat flux are mounted 300 mm above the nozzle centerline.

Fig. 3 Heat model/model support system.

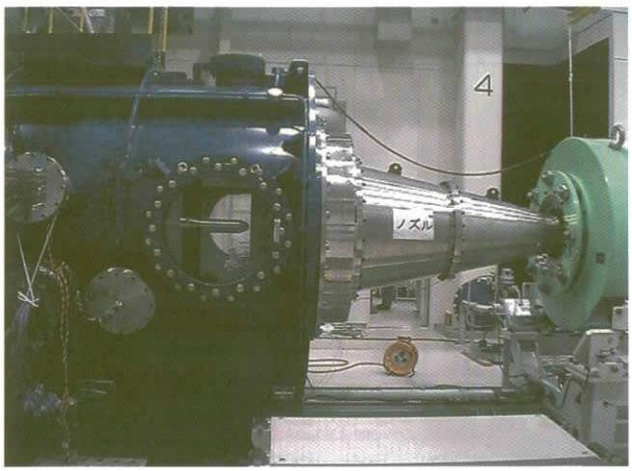

Fig. 4 Nozzle/test section overview.

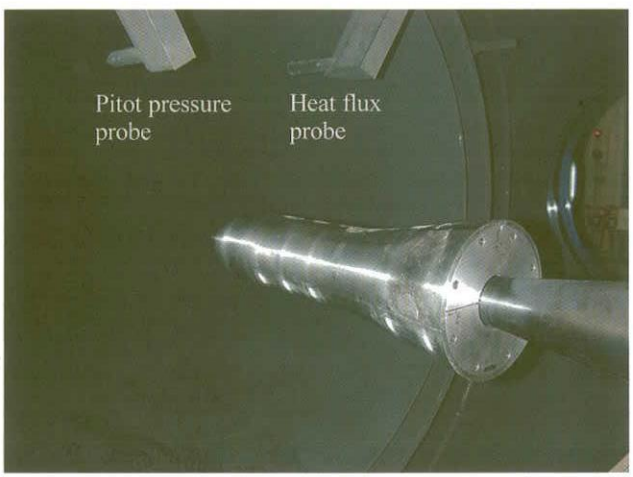

Fig. 5 Heat model installed in the test section.

4.2 Data acquisition/reduction

Generally, aerodynamic force measurement in an impulse facility such as a shock tunnel includes a number of problems due to extremely short flow duration times. As a flow takes place, the model and its support system impulsively respond to the flow onset and keep vibrating over the measurement time. In order to extract actual aerodynamic force from data including such oscillating components, an acceleration compensation technique using accelerometers was applied in the present study.

By assuming rigid body, the axial force F_x acting on a model can be expressed as

$$F_x = kx + ma \tag{1}$$

where k, x, m, and a denote the main coefficient of balance, balance voltage output, equivalent inertia mass, and acceleration of the model, respectively. Hence the force data , which includes vibration component, can be compensated by applying the above relation together with the acceleration data a measured from the accelerometers. The equivalent inertia mass m can be reduced from dynamic calibrations using a fracture-stick. In order to remove random noise components, both balance voltage and accelerometer data were smoothed with a moving average filter.

Next, the following empirical formula provides a relation between the free stream dynamic pressure $q_\infty = \rho_\infty u_\infty^2 /2$ and the Pitot pressure

$$\rho_\infty u_\infty^2 = \begin{cases} 1.073\, P_{\mathrm{pit}} & H_0 = 4\ \mathrm{MJ/kg} \\ 1.064\, P_{\mathrm{pit}} & H_0 = 8 - 11\ \mathrm{MJ/kg} \end{cases} \tag{2}$$

The difference of the factor comes from the degree of real gas effects on the specific heat between the two enthalpy levels. Therefore the dynamic pressure is reduced from the Pitot pressure data measured from the permanent probe. The aerodynamic force is then converted to the axial force coefficient defined as

$$C_A = \frac{F_x}{q_\infty A} \tag{3}$$

where $A = \pi D^2 /4$ is the reference area. Finally, the time series of axial force coefficient data calculated from Eqs. (1)-(3) is averaged in time with an averaging interval of 2 msec (e.g., from 2.5 to 4.5 msec of the measurement time for 4 MJ/kg data). No base pressure correction was performed in the present test although it has been reported in the HWT test [1] that the effect of base pressure correction to the total value can reach as much as 4%.

For the heat flux measurements, the junction of the thermocouple sensor (expected to be located near the chromel/constantan border) was made by scratching the surface using sandpaper and the time history of the sensor voltage was recorded using a data recorder. The voltage data were recorded at a sampling frequency of 500 kHz. In order to remove noise components, data were smoothed by applying the first-order least square fitting technique at each sampling point with a fitting interval of 2 msec

(note that the moving average corresponds to the zeroth-order least square fitting). The smoothed sensor voltage was then converted to temperature using a polynomial expression which relates the thermoelectric voltage to temperature. To reduce aerodynamic heating from the thermocouple data, it is assumed that 1) heat conduction along the body surface is negligible and 2) thermal properties are not dependent on temperature. Denoting the temperature measured at each time step (t_0, t_1, $\cdots$, t_n) as ($T(t_0)$, $T(t_1)$, $\cdots$, $T(t_n)$), we can evaluate the model surface heat flux at time t_n by applying the formula of Cook and Felderman [6], [7], which is written as

$$q(t_n) = 2\sqrt{\frac{\rho c k}{\pi}} \sum_{i=1}^{n} \frac{T'(t_i) - T'(t_{i-1})}{\sqrt{t_n - t_i} + \sqrt{t_n - t_{i-1}}} \qquad (4)$$

where T' denotes temperature increment from the initial value, i.e., $T'(t_i) = T(t_i) - T(t_0)$. The thermal effusivity defined as $\sqrt{\rho c k}$ was specified as an averaged value of chromel and constantan at a reference temperature of 100°C ($\sqrt{\rho c k}$ = 8918.6 $Ws^{1/2}/m^2K$). Finally, the computed time history of the heat flux was averaged in time to produce a time-averaged value for each shot.

5. RESULTS AND DISCUSSION

5.1 Force tests

As described in the previous section, to perform the acceleration compensation, the model equivalent inertia mass m was determined from the dynamic calibration tests using a fracture stick. Figure 6 (a) shows the time history of the balance axial force kx and acceleration a (averaged value between the two accelerometers) obtained in the present calibration test. From the figure, it is seen that the acceleration shows an opposite phase to the balance axial force. The inertia mass was then reduced from the spectral ratio of kx and a together with the natural vibration frequency of the balance system in the axial direction (1.22 kHz). A total of 5 calibration tests were performed and the averaged inertial mass was evaluated as 6.25 kg, which is very close to the sum of balance attachment weight (1.5 kg) and the model weight (4.78 kg). Figure 6 (b) shows the time variation of the reconstructed axial force expressed as $F_x = kx + ma$. It is confirmed that the axial force converges to zero as expected.

By using the inertial mass obtained, the axial force coefficient can be reduced from Eq. (1) to Eq. (3), together with the balance/accelerometer output and Pitot pressure measured at each shot. Shown in Figs. 7, 8, and 9 are typical time variations of axial force, Pitot pressure, and the axial force coefficient for the three enthalpy levels of 4, 8, and 11 MJ/kg (condition A, D, and E in Table 1). In order to average the axial coefficient data in

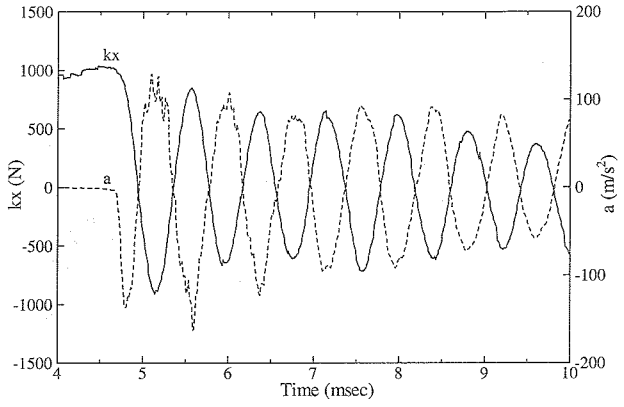

(a)

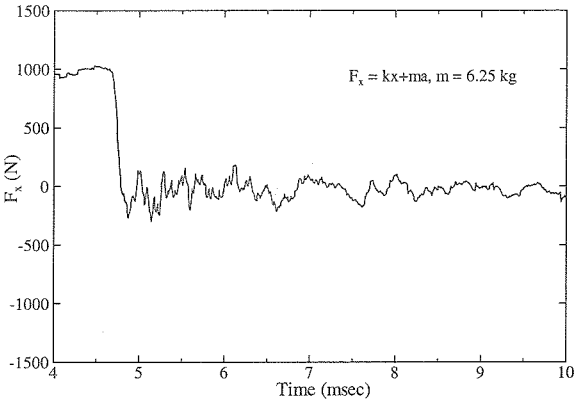

(b)

Fig. 6 Results of fracture stick calibration test.
(a) Balance output and acceleration
(b) Recovered axial force

time, a test window of 2 msec was chosen from 2.0-2.5 msec after the flow initiation time, when the Pitot pressure and axial force were found to have settled down. Because of the relatively low stagnation pressure (i.e., small balance output), the aerodynamic coefficient data for the enthalpy level of 4 MJ/kg includes many random components compared to the other two enthalpy levels. As confirmed from Fig. 7 (a), the level of force output in this case is at most 100 N, which is much smaller compared to the balance capacity for the axial direction (980 N). Hence the data inevitably includes a series of noise components which cannot be removed even by using the present data reconstruction technique. On the other hand, the data of H_0 = 8 MJ/kg shows the largest axial force output because of the high stagnation pressure (see Table 1), and the axial force coefficient indicates almost a constant value around the time of 3 msec.

Next the time-averaged axial coefficients are plotted as a function of the viscous interaction parameter $\bar{v}_\infty$ defined as

$$\bar{v}_\infty = \frac{M\sqrt{C_\infty}}{\sqrt{\mathrm{Re}}} \qquad (5)$$

where $C_\infty = \mu_w T_\infty / \mu_\infty T_w$ is the Chapman-Ruebesin constant

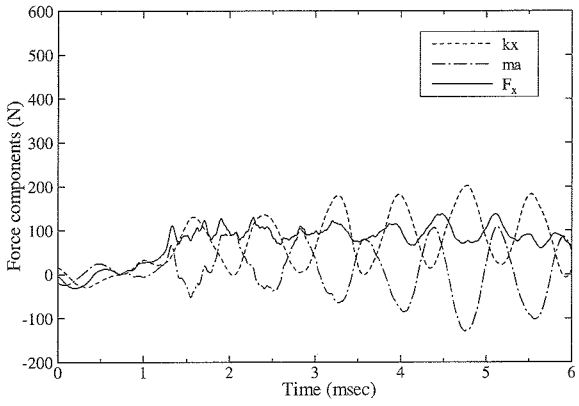

(a)

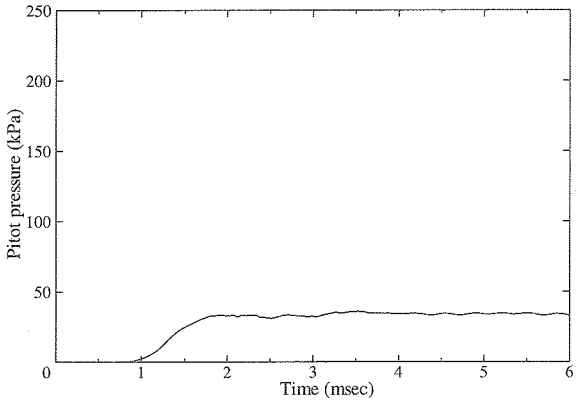

(b)

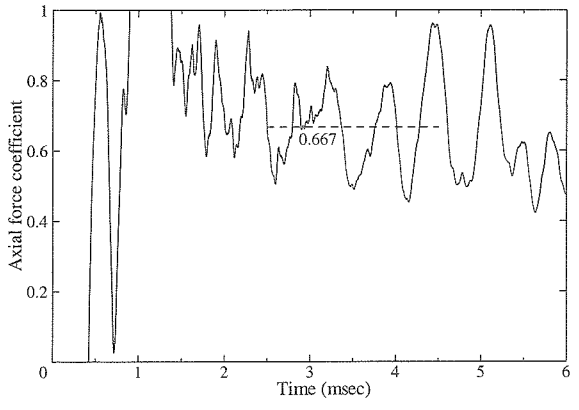

(c)

Fig. 7 Measured time histories for shot 406 (H_0 = 4 MJ/kg).
(a) Balance output, acceleration, and recovered axial force
(b) Pitot pressure
(c) Axial force coefficient

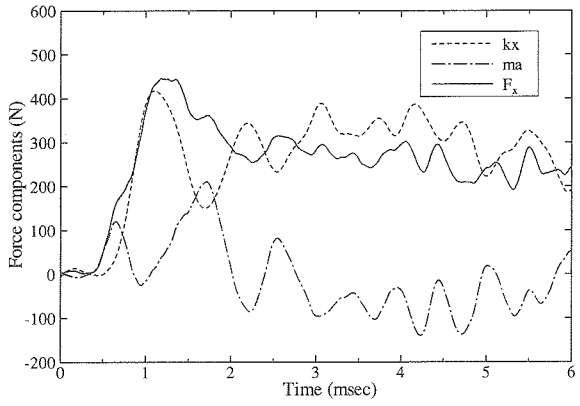

(a)

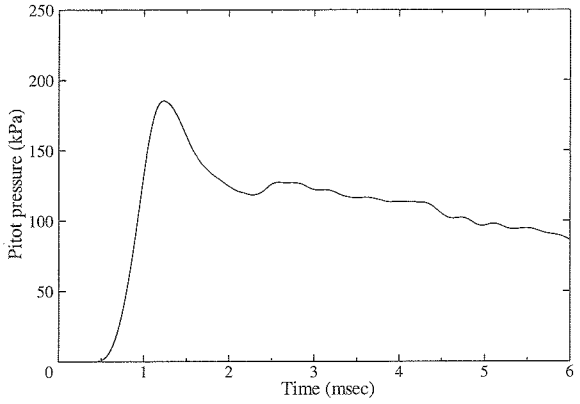

(b)

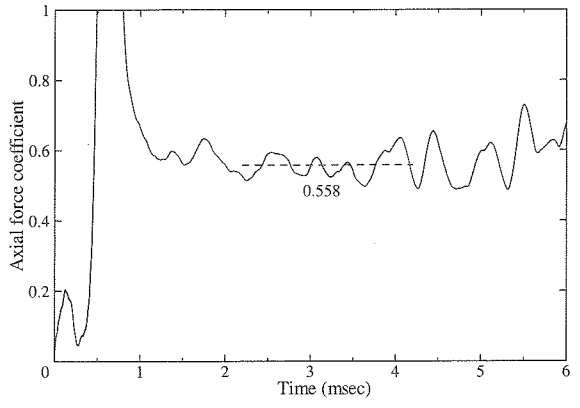

(c)

Fig. 8 Measured time histories for shot 402 (H_0 = 8 MJ/kg).
(a) Balance output, acceleration, and recovered axial force
(b) Pitot pressure
(c) Axial force coefficient

and assumed to be unity. The data are also compared with data obtained at the HWT, Arnold Engineering Development Center (AEDC) von Kármán Gas Dynamics Facility (VKF) Hypersonic Wind Tunnel (C), and AEDC VKF Hypervelocity Wind Tunnel (H) in Fig. 10. As already mentioned, the data of HWT was taken from wind tunnel tests performed as a series of the present comparative test campaigns and summarized in detail in Ref. [1]. Since HWT is a blow-down type cold wind tunnel, the stagnation enthalpy attainable in this facility is at most 1 MJ/kg and hence real gas effects are expected to be negligible. The stagnation pressure and corresponding Mach number and Reynolds number based on the centerbody diameter of the model are 1 MPa, 9.5, and 1.0×10^5, respectively. Under these conditions, the viscous interaction parameter becomes almost identical to the value obtained in HIEST at the enthalpy of 4 MJ/kg.

The data of AEDC wind tunnels were cited from Ref. [3]. Both

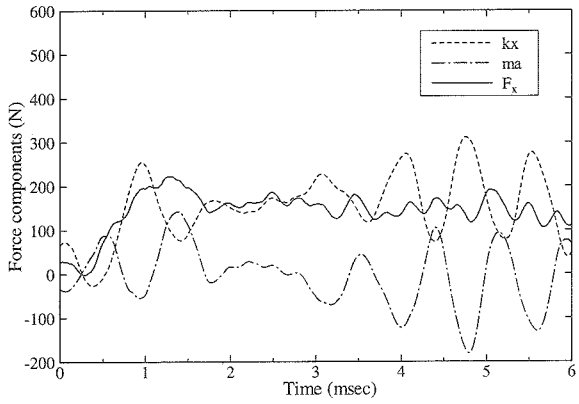

(a)

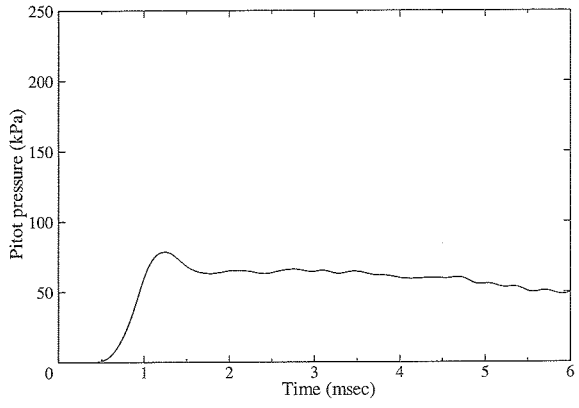

(b)

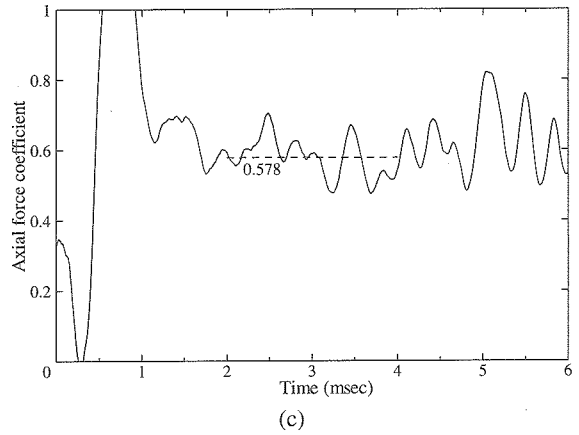

(c)

Fig. 9 Measured time histories for shot 410 (H_0 = 11 MJ/kg).
(a) Balance output, acceleration, and recovered axial force
(b) Pitot pressure
(c) Axial force coefficient

AEDC tunnels are also blow-down type wind tunnels and the stagnation temperature of the VKF (C) tunnel is around 1000 K and is almost same as in HWT. In the VKF (H) tunnel, a free stream Mach number of up to 20 can be attained, and a relatively low Reynolds number range from 1.7×10^4 to 6.8×10^4 results in a large viscous interaction parameter.

Note that the HWT data are zero-lift axial force coefficient defined as

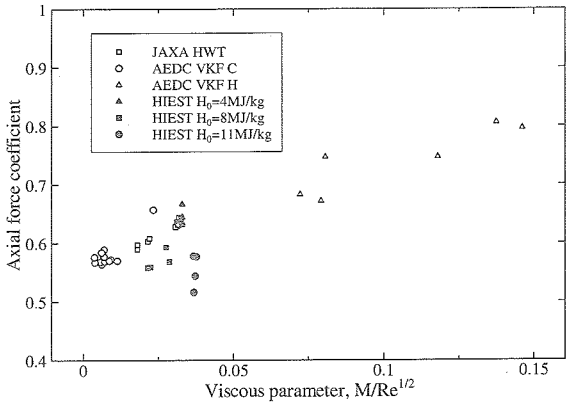

Fig. 10 Comparison of axial force coefficient with other wind tunnel data as a function of viscous interaction parameter.

$$C_{AF} = C_A - \frac{(p_\infty - p_b) A_b}{q_\infty A} \tag{6}$$

where p_b and A_b denotes the base pressure and model base area, respectively. From the HWT tests, it has been found that the zero-lift axial force coefficient is typically around 2% lower than the total axial force coefficient. The quantitative impact of the base pressure contribution on axial force coefficient for the present test conditions is yet to be determined.

As can be seen from Fig. 10, the HIEST data of H_0 = 4 MJ/kg indicates a reasonable correlation with the HWT/VKF tunnel data. On the contrary, the data for higher enthalpy cases noticeably deviate from the correlation trend. Since the degree of deviation becomes larger as the enthalpy increases, it is conceivable that this is caused by real gas effects.

To extract the real gas effect contribution, we assume that the axial force coefficient can be expressed by the following form

$$C_A = C_{A,\text{ideal}} + \Delta C_{A,\text{vis}} + \Delta C_{A,\text{real}} \tag{7}$$

where $C_{A,\text{ideal}}$ is the coefficient for ideal (i.e., inviscid) flow, $\Delta C_{A,\text{vis}}$ the contribution for the viscous interaction effects, and $\Delta C_{A,\text{real}}$ the contribution for the real gas effect. Since the flow of HWT and VKF can be treated as thermally perfect, the first two terms in Eq. (7) can be modelled by correlating these data and expressed as a function of viscous parameter, which results in

$$C_{A,\text{ideal}} + \Delta C_{A,\text{vis}} = 0.556 + 2.505 \frac{M_\infty \sqrt{C_\infty}}{\sqrt{\text{Re}}} \tag{8}$$

Therefore the real gas contribution $\Delta C_{A,\text{real}}$ is estimated by subtracting Eq. (8) from Eq. (7) for each enthalpy level. The relation of $\Delta C_{A,\text{real}}$ versus the stagnation enthalpy is plotted in Fig. 11. Generally, even in the case of H_0 = 11 MJ/kg, the stagnation tem-

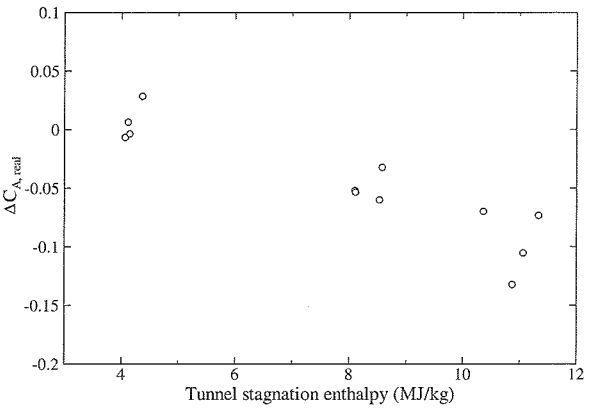

Fig. 11 Estimated real gas e.ects for axial force coefficient versus tunnel stagnation enthalpy.

perature is not sufficiently high enough to dissociate air and hence a series of real gas effects are considered to be relatively minor. However, Fig. 11 clearly indicates that the axial force coefficient significantly decreases as the stagnation enthalpy increases. It is uncertain whether the real gas effects are primary responsible for this trend, but there is a possibility that the change in pressure distribution on the flare part due to dissociation decreased the axial force. Since the flow behind a bow shock wave at the cone/flare part is supersonic, dissociation acts so as to decrease the pressure. As far as the axial force is concerned, the pressure distribution on the flare plays a dominant role in determining total pressure drag. Therefore the pressure decrease in the flare part may noticeably change the axial force coefficient even though the degree of dissociation is low. A detailed CFD analysis is expected to give useful information for understanding the basic mechanism of such real gas effects and this will be addressed in the near future.

Finally, the tunnel conditions and corresponding axial force coefficient data for each shot are summarized in Table D1 of Appendix D.

5.2 Heat tests

For the heat tests, the flow field was visualized by the Schlieren technique and typical photographs for the two enthalpy levels of 4 and 8 MJ/kg (condition A and B in Table 1) are indicated in Figs. 12 (a) and (b). Concerning the shock shape, notable differences are not observed between the two conditions.

As previously mentioned, data repeatability was examined for the two enthalpy levels by conducting a total of 17 shots (10 and 7 shots for the 4 and 8 MJ/kg cases, respectively). In Figs. 13 and 14, time histories of sensor output and heat flux for the sensor corresponding to the stagnation point (sensor 4 in Fig. A2) for the shots 376 and 379 are shown. Note that the stagnation enthalpy and pressure are almost identical for these two shots (see Table

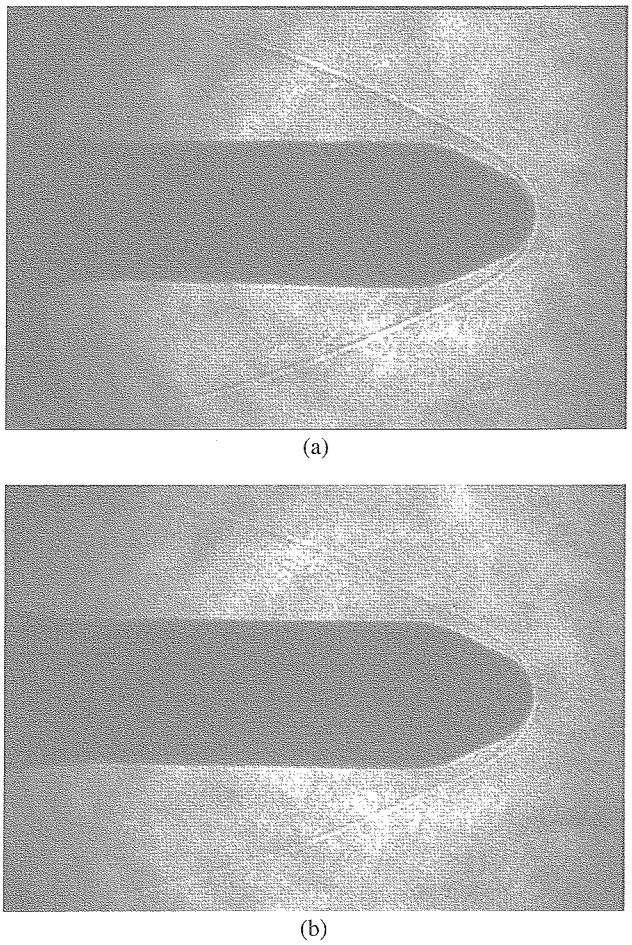

(a)

(b)

Fig. 12 Heat test schlieren photograph.
(a) H_0 = 4 MJ/kg (Shot 379)
(b) H_0 = 8 MJ/kg (Shot 388)

D2 of Appendix D). For Fig. 13, the heat flux indicates almost a constant value after the flow field is established. The noise temporary observed at the time around 2 ms is probably due to the electrical disturbance caused by impingement of the starting shock wave to the sensor cables. On the other hand, very noisy output all through the measurement time is observed for the shot 379 in Fig. 14, although the tunnel conditions are almost the same as 376. Such noisy data were observed only for the nose part (sensor 1-9 in Fig. A2) and not for sensors in the cylinder/flare part. Considering this, we can mention that one probable cause of this is the impingement of flow contaminations such as the second diaphragm placed in the throat. In fact, a number of scratches were observed on the model surface after the shots of 4 MJ/kg case as can be seen in Fig. 15. Since these noisy data were observed only at the enthalpy level of 4 MJ/kg and not at 8 MJ/kg, there is a possibility that the free stream temperature at H_0 = 4 MJ/kg is not high enough to vaporize the diaphragm.

Next the comparison of the time-averaged heat flux data between the model and permanent probe at the stagnation point

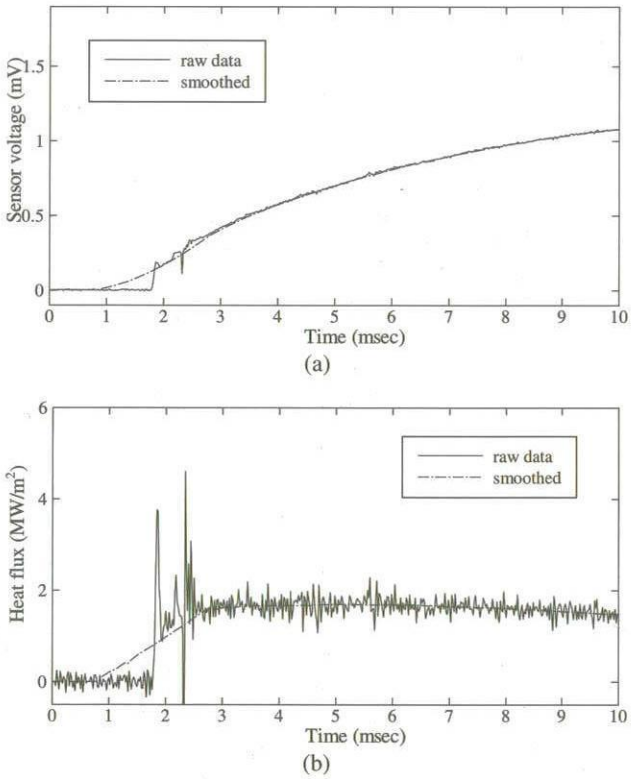

Fig. 13 Measured time history at the stagnation point for shot 376.
(a) Sensor output
(b) Heat flux

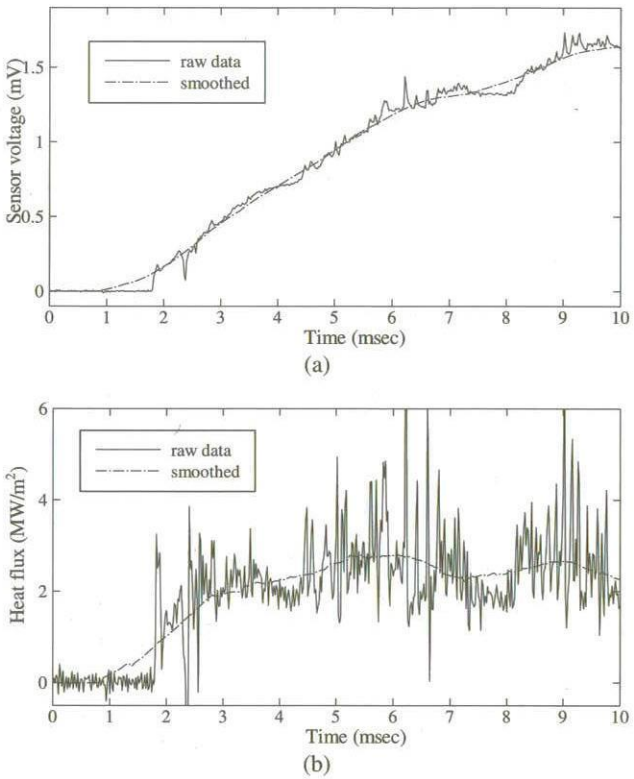

Fig. 14 Measured time history at the stagnation point for shot 379.
(a) Sensor output
(b) Heat flux

for each shot are tabulated in Table 2. These two data points are compared by assuming that the stagnation point heat flux varies inversely with the square root of the nose radius. The validity of this assumption is examined via a CFD analysis in Appendix B. It should be noted that the data from shots 378, 379, 381, and 385 include large noise components due to the flow contamination discussed in the previous paragraph and hence they are not included. It is confirmed from Table 2 that the permanent probe data typically exceeds the model data. From the previously performed flow calibration test, it was observed that the Pitot pressure at the point 250-300 mm from the nozzle center line is around 5% higher than averaged value for the case of H_0 = 4 MJ/kg. Hence it is conceivable that the flow non-uniformity in the radial direction is a cause of this discrepancy. The effect of model/probe surface roughness is also a non-negligible factor to cause a measurement error. In addition, uncertainty concerning the depth of the thermocouple junction is another possibility. It has been pointed out that as much as 30% of uncertainty can be caused in a short duration test facility if the thermocouple junction is 0.1 mm deep into the body surface. This is further discussed in Appendix C. In any case, the data variation for each shot is normally kept within 5% and hence the data repeatability of the present test is found to be satisfactory.

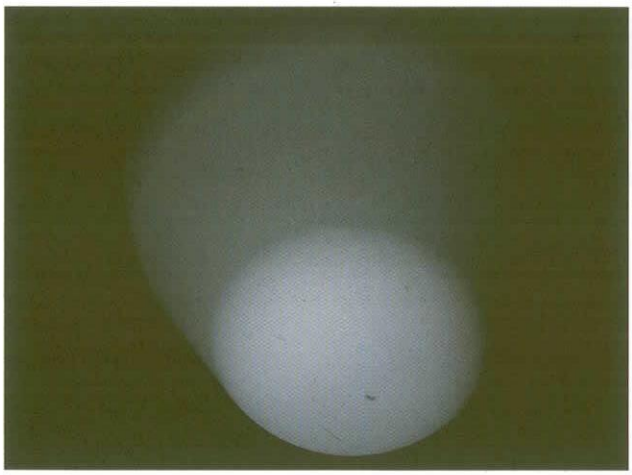

Fig. 15 Close-up view of heat model nose part after the shot.

Figures 16 (a) and (b) show an example of the comparison with the data obtained at the HWT heat test for the normalized (divided by the stagnation value) heat flux distribution along the model surface. As earlier stated, the same model as used in the present test was used in the HWT tests. The stagnation enthalpy and Reynolds number of HWT in this case is 1 MJ/kg and 2×10^6 1/m, respectively. A detailed description of the HWT data is found in Ref. [1]. The error bar for the HIEST data indicated in

Table 2 Comparison of the stagnation point heat flux between the model and permanent probe

Shot No.	376	377	380	382	383	384	386	387	388	389	390	391	392
q_{model} (MW/m^2)	1.679	1.888	1.800	1.740	1.920	1.700	4.540	4.510	4.140	4.360	4.290	4.040	1.940
q_{probe} (MW/m^2)	2.829	3.002	3.360	3.292	3.399	3.322	9.186	8.456	7.617	7.761	8.571	7.781	3.475
q_{model}/q_{probe} *	1.028	1.090	0.928	0.915	0.978	0.886	0.856	0.924	0.941	0.973	0.867	0.899	0.967

* rescalled by square root of the nose radius

Fig. 16 means the random uncertainty (precision limit) for the normalized value and was evaluated as

$$\Delta\left(\frac{q}{q_{stg}}\right)=\sqrt{\left(\frac{1}{q_{stg}}\Delta q\right)^2+\left(\frac{q}{q_{stg}^2}\Delta q_{stg}\right)^2} \tag{9}$$

where, for example, $\Delta q = 2\sigma$ and σ is the standard deviation. In Fig. 16, a good agreement of typically within several percent is noted for sensors in the nose part where the level of heat flux is relatively high. This trend holds both for H_0 = 4 and 8 MJ/kg cases, implying that the change of stagnation enthalpy has little effect on the normalized heat flux distribution. In other words, it can be confirmed that, as far as the present test conditions are concerned, it is reasonable to compare the present HIEST data with HWT although the tunnel conditions are different for each other. On the other hand, in the cylinder part, there is a discrepancy compared to the HWT data since the sensor output frequently suffers from large random noise components due to low heating.

Finally, details of the present heat test data and corresponding tunnel conditions are summarized in Table D2 of Appendix D.

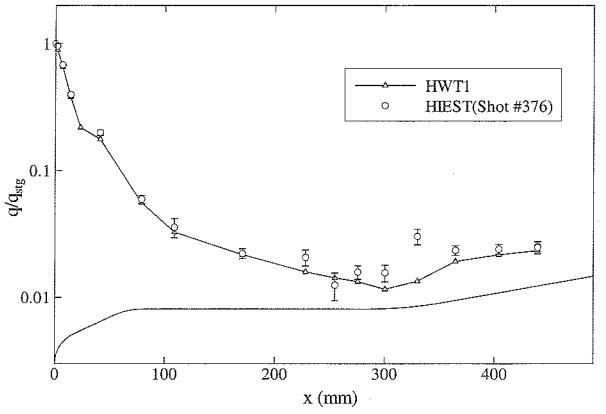

(a)

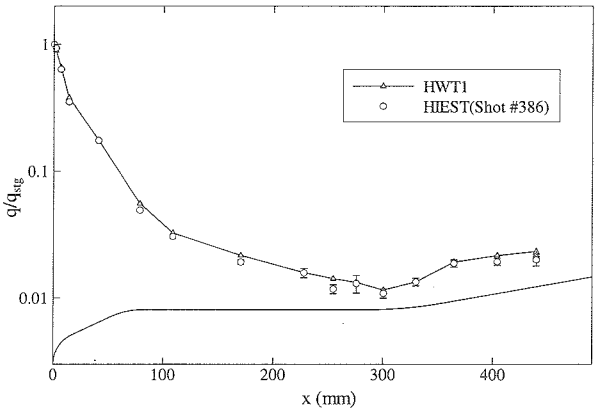

(b)

Fig. 16 Comparison of non-dimensional heat flux distribution between HIEST and HWT data.
(a) H_0 = 4 MJ/kg (Shot 376)
(b) H_0 = 8 MJ/kg (Shot 386)

6. CONCLUSIONS

As a series of comparative test campaigns between two hypersonic test facilities in JAXA, force and heat flux measurements were conducted at the High Enthalpy Shock Tunnel, HIEST. A ballistic type configuration designated as HB-2 was employed for the model and the test was conducted at the tunnel stagnation enthalpy levels of 4, 8, and 11 MJ/kg for the force tests and 4 and 8 MJ/kg for the heat tests.

For the force tests, axial force was measured by using a cross-beam type three-component balance and was converted to the aerodynamic coefficient by recovering the data to remove vibration components through an acceleration compensation technique. It has been found that the present compensation technique can reasonably recover the original data and extract meaningful information. By plotting the axial force coefficient as a function of the viscous interaction parameter, a good correlation with available data obtained at other hypersonic test facilities was confirmed for the case of H_0 = 4 MJ/kg. On the other hand, the data for the enthalpy levels of 8 and 11 MJ/kg slightly deviated from the correlation trend for reasons as yet to be determined, possibly due to real gas effects.

For the heat tests, temperature data were recorded using chromel-constantan type co-axial thermocouples and were numerically integrated in time to determine the surface heat flux by applying one-dimensional heat conduction theory. The stagnation point heat flux data showed good repeatability, within 5% both for the enthalpy levels of 4 and 8 MJ/kg.

The comparison of the normalized heat flux distribution in the nose part of the model showed the present data to be within several percent of measurements obtained at a blowdown-type cold

wind tunnel, indicating that reliable data were obtained in HIEST from a qualitative viewpoint. The effect of the stagnation enthalpy difference on the heat flux distribution was found to be negligible in the range of the present flow conditions.

Finally, the present force/heat test results are believed to provide useful information as a database for hypersonic/high-enthalpy test facilities and for the validation of hypersonic CFD codes.

ACKNOWLEDGMENTS

The authors would like to thank Mr. Takuya Maehara and Mr. Tomoaki Narita of the Foundation for Promotion of Japanese Aerospace Technology (JAST) for their contributions to the present tests.

REFERENCES

1) Kuchi-Ishi, S., Watanabe, S., Nagai, S., Tsuda, S., Koyama, T., Hirabayashi, N., Sekine, H., and Hozumi, K., "Comparative Force/Heat Flux Measurements between JAXA Hypersonic Test Facilities Using Standard Model HB-2 (Part 1: 1.27 m Hypersonic Wind Tunnel Results)," JAXA Research and Development Report JAXA-RR-04-035E, 2005.
2) Itoh K., Ueda, S., Komuro T., Sato, K., Tanno, H., and Takahashi, M., "Hypervelocity Aerothermodynamic and Propulsion Research Using a High Enthalpy Shock Tunnel HIEST," AIAA Paper 99-4960, 1999.
3) Gray, J. D., "Summary Report on Aerodynamic Characteristics of Standard Models HB-1 and HB-2," AEDC-TDR-64-137, July 1964.
4) Kidd, C.T., Nelson C.G., and Scott, W.T., "Extraneous Thermoelectric EMF Effects Resulting from the Press-Fit Installation of Coaxial Thermocouples in Metal Models," *Proceedings of the 40th International Instrumentation Symposium,* Baltimore, MD, May 1994, pp. 317-335.
5) Lordi, J.A., Mates, R.R., and Moselle, J.R., "Computer Program for the Numerical Solution of Nonequilibrium Expansions of Reacting Gas Mixtures," NASA CR-472, 1966.
6) Cook, W. J., and Felderman, E. J., "Reduction of Data from Thin-Film Heat-Transfer Gages: A Concise Numerical Technique," *AIAA J.*, Vol. 4, No. 3, March 1966, pp. 561-562.
7) Schultz, D.L., and Jones, T. V., "Heat Transfer Measurements in Short Duration Hypersonic Facilities," AGARDograph 165, 1973.
8) Fay, J. A. and Riddell, F. R., "Theory of Stagnation Heat Transfer in Dissociated Air," *Journal of Aeronautical Sciences*, Vol. 25, No. 2, Feb. 1958, pp. 73-85.
9) Anderson, Jr., J. D., *Hypersonic and High Temperature Gas Dynamics*, McGraw-Hill, New York, 1989, p. 635.
10) Kuchi-Ishi, S., "The Development of a New Viscous Shock-Layer Code for Computing Hypersonic Flows around Blunted Body and Its Applications," JAXA Research and Development Report JAXA-RR-05-001E, 2005.

Appendix A
Detail of the force/heat model

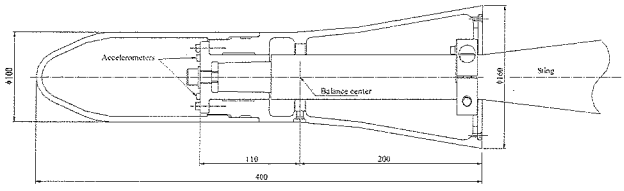

Fig. A1 Detailed drawing of HB-2 force model.

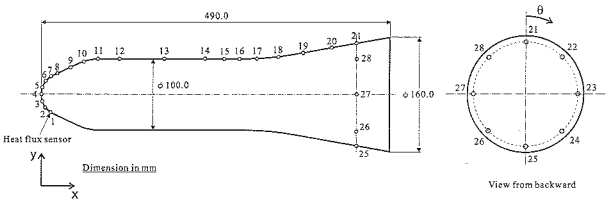

Fig. A2 Sensor location of HB-2 heat model.

Table A1 Heat flux sensor location

Sensor No.	x (mm)	y (mm)	θ (deg)
1	13.9	-25.3	0.0
2	6.5	-18.6	0.0
3	1.7	-9.9	0.0
4	0.0	0.0	0.0
5	1.7	9.9	0.0
6	6.5	18.6	0.0
7	13.9	25.3	0.0
8	22.9	29.8	0.0
9	41.0	38.2	0.0
10	59.3	46.3	0.0
11	78.9	49.9	0.0
12	108.9	50.0	0.0
13	170.7	50.0	0.0
14	228.1	50.0	0.0
15	254.8	50.0	0.0
16	275.6	50.0	0.0
17	300.4	50.3	0.0
18	329.8	52.5	0.0
19	364.6	57.9	0.0
20	404.0	64.9	0.0
21	439.3	71.1	0.0
22	439.3	50.3	45
23	439.3	0.0	90
24	439.3	-50.3	135
25	439.3	-71.1	180
26	439.3	-50.3	225
27	439.3	0.0	270
28	439.3	50.3	315

Appendix B
On the relation between the stagnation point heat flux and nose radius of a hemisphere

In section 5.2, the stagnation point heat flux data were compared between the model and the permanent probe by assuming that they are inversely proportional to the square root of the nose radius. This relation can be derived from the theoretical formula of Fay and Riddell [8], together with the velocity gradient at the boundary layer edge given from the Newtonian flow theory [9]. In order to examine as to whether this theoretical relation is valid in the present test conditions, a numerical analysis was made by using a Viscous Shock-Layer (VSL) code.

The VSL technique can solve hypersonic flows around a blunt body both quickly and accurately. This equation system is derived from the steady-state Navier-Stokes (NS) equations by keeping terms up to second order in the inverse square root of the Reynolds number. Although an approximate method of solving the NS equations, the VSL technique can produce essentially identical results compared to the NS solution for a certain flow conditions of interest. In the present analysis, a set of stagnation point heat flux data for various nose radii were obtained and the results were correlated in terms of the nose radius. The code used in this analysis was previously developed by one of the present authors and its detailed description is found in Ref. [10].

The VSL analysis was performed for the condition of H_0 = 4 MJ/kg with a perfect gas assumption by incrementally changing the nose radius from 10 to 30 mm, according to the actual values of the permanent probe and model. Figure B1 shows the stagnation point heat flux obtained from the VSL code versus the nose radius together with a correlated curve. The result clearly indicates that the stagnation point heat flux can be expressed very well as a function of the inverse square root of the nose radius.

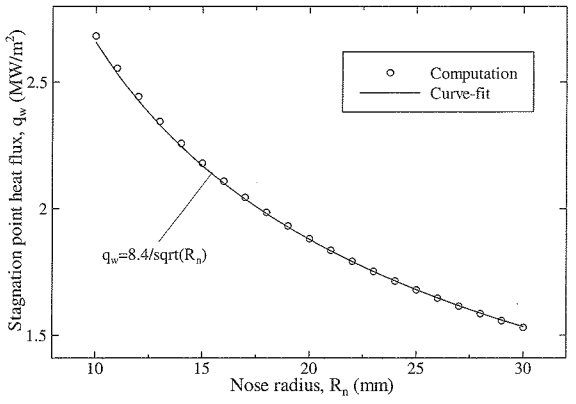

Fig. B1 Relation between the stagnation point heat flux and the nose radius of hemisphere for the HIEST condition of H_0 = 4 MW/m^2.

Dividing the heat flux for the nose radius of 10 mm by 30 mm, we can have a value of 1.752, which is only 1% different from $\sqrt{3}$ and much smaller than the experimental uncertainty. Hence it has been confirmed that it is reasonable to compare the stagnation heat flux data between the model and the permanent probe by rescaling the data with the inverse square root of the nose radius.

Appendix C
On the effect of thermocouple junction depth

The depth of the point at which the thermocouple junction is made can have an impact on the accuracy of heat flux measurements. Ideally, the junction should be made exactly on the top surface of the sensor. However, since the junction is made by hand using sandpaper, it could be made away from the surface. In this case, we are obliged to record the temperature variation inside the material, not on the surface. This can become an error source of the heat flux reduction process and hence the effect of the junction depth was numerically investigated herein with the aid of one-dimensional heat conduction theory.

By assuming constant heating q_0 for a semi-infinite medium, the temperature variation at a distance x from the surface and a time t can be expressed as [7]

$$T - T_i = \frac{2q_0}{k}\sqrt{\frac{\alpha t}{\pi}}\exp\left(\frac{-x^2}{4\alpha t}\right) - \frac{q_0 x}{k}\left[1 - \mathrm{erf}\left(\frac{x}{2\sqrt{\alpha t}}\right)\right] \quad \text{(B1)}$$

where T_i is the initial temperature, $\alpha = k/\rho c$ the diffusivity of the material, and erf() the error function. In the present analysis, the temperature variation obtained from the above equation with q_0 = 1 MW/m^2 was numerically integrated to reduce the heat flux time history by using Eq. (4) for the three x of 0, 10, and 100 μm. Shown in Figs. B1 (a) and (b) are the comparison of the temperature/heat flux time history between the three distances. For x = 0 μm, the heat flux instantaneously reaches a constant value of 1 MW/m^2 as anticipated. On the other hand, for x = 100 μm, as much as 30% of difference from the surface value can be observed at t = 5 ms. This implies that a 30% measurement error can occur if the thermocouple junction is made 100 μm away from the surface. Even for x = 10 μm, the error can reach up to 3%.

Since the extent of temperature increase is proportional to q_0 as confirmed from Eq. (B1), the degree of uncertainty discussed above is not dependent on the level of heat flux; it is a function of t and x only. If the measurement time becomes of the order of 1 s such as in a blow-down type wind tunnel, this kind of error is insignificant because the temperature variation becomes almost identical between the top surface and the locations slightly away from the surface. However, for shock tunnels, the time scale of heat flux measurement is of the order of milliseconds and in this case we cannot ignore the effect of the junction depth as confirmed in Fig. (B1). Needless to say, there is no way to check the junction depth for actual wind tunnel tests, but we can at least point out that the surface junction depth uncertainty can have an enormous impact on the accuracy of heat flux measurement in a short-duration facility.

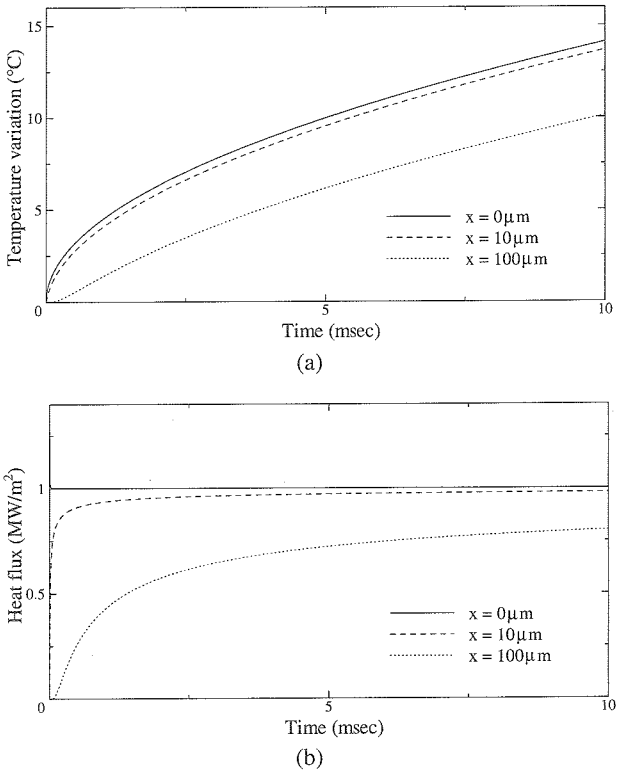

Fig. C1 Comparison of temperature/heat flux time variation between three levels of distance from the sensor surface.
(a) Temperature
(b) Heat flux

Appendix D
Summary of the force/heat test results

Following is a summary of the present force/heat test data together with the tunnel conditions for each shot. Note that free-stream conditions are not included in the table although they can be obtained from the measured tunnel reservoir conditions through the use of a one-dimensional nozzle flow code. In order to serve the present data as a database for CFD validation, a novel approach that can produce more reliable free-stream properties should be developed and this is to be addressed in the near future.

Table D1 Summary of force test results

Shot No.	Condition	P_0 (MPa)	V_{sh} (m/s)	H_0 (MJ/kg)	P_{pit} (kPa)	Throat (mm)	C_A
402	D	47.02	2729.0	8.10	119.7	50	0.558
403	D	43.71	2760.1	8.11	116.0	50	0.559
404	C	42.16	2874.0	8.53	77.6	40	0.568
405	C	45.46	2853.3	8.58	77.1	40	0.593
406	A	17.64	1926.6	4.37	33.9	40	0.667
407	A	13.61	1905.1	4.06	30.1	40	0.632
408	A	14.76	1918.4	4.11	29.5	40	0.645
409	A	13.95	1924.6	4.14	29.3	40	0.635
410	E	30.17	3131.4	10.36	63.9	40	0.578
411	E	31.17	3230.3	10.87	68.0	40	0.516
412	E	31.02	3313.4	11.33	63.7	40	0.577
413	E	31.17	3257.8	11.06	68.4	40	0.544

Table D2 Summary of heat test results

Shot No.	376	377	378	379	380	381	382	383	384	385	386	387	388	389	390	391	392
P_0 (MPa)	15.59	15.65	15.39	15.11	15.19	15.48	15.45	15.05	15.20	23.10	22.72	23.06	22.78	23.17	23.08	22.81	15.03
V_{sh} (m/s)	1943.9	1961.0	1947.0	1926.3	1958.9	1950.3	1967.9	1953.3	1949.5	2705.3	2623.6	2666.0	2695.2	2790.8	2798.9	2717.6	1983.1
H_0 (MJ/kg)	4.33	4.38	4.30	4.28	4.34	4.30	4.39	4.35	4.27	7.70	7.51	7.68	7.79	8.17	8.23	7.80	4.43
P_{pit} (kPa)	30.62	30.93	29.66	29.41	30.19	30.23	30.68	29.83	30.62	46.90	44.71	45.65	44.44	46.00	44.23	44.85	29.63

Sensor No.	Heat Flux (MW/m^2)																
1	0.637	0.675	0.742*	0.918*	0.685	0.742*	0.689	0.714	0.634	1.940	1.570	1.540	1.480	1.610	1.830	1.460	0.691*
2	1.238	1.332	1.360*	1.620*	1.230	1.369	1.220	1.300	1.130	4.500*	2.930	2.910	2.690	2.800	2.750	2.690	1.230
3	1.822	1.890	2.160*	2.170*	1.690	1.885	1.690	1.820	1.610	5.770*	4.370	4.290	3.880	4.200	4.010	3.840	1.790
4	1.679	1.888	2.250*	2.400*	1.800	4.613*	1.740	1.920	1.700	5.700*	4.540	4.510	4.140	4.360	4.290	4.040	1.940
5	1.609	1.724	1.990*	2.150*	1.640	1.877	1.650	1.790	1.560	5.760*	4.250	4.170	3.750	3.940	3.770	3.610	1.750
6	1.141	1.202	1.340*	1.540*	1.160	1.328	1.170	1.250	1.100	4.370*	2.890	2.860	2.630	2.730	2.690	2.610	1.200
7	0.666	0.696	0.783	0.909	0.661	0.827	0.681	0.726	0.637	1.960	1.600	1.690	1.570	1.600	1.570	1.620	0.696
9	0.333	0.361	0.399	0.956*	0.352	0.444	0.354	0.362	0.338	0.870	0.793	0.847	0.794	0.884	0.840	0.779	0.370
11	0.099	0.101	0.097	0.100	0.100	0.093	0.098	0.095	0.091	0.214	0.224	0.223	0.215	0.216	0.209	0.199	0.091
12	0.060	0.062	0.060	0.061	0.060	0.059	0.058	0.058	0.057	0.135	0.139	0.138	0.147	0.142	0.140	0.141	0.064
13	0.037	0.036	0.037	0.042	0.040	0.039	0.037	0.034	0.035	0.082	0.087	0.083	0.090	0.090	0.086	0.084	0.037
14	0.035	0.027	0.030	0.030	0.030	0.030	0.035	0.033	0.036	0.071	0.072	0.072	0.078	0.072	0.070	0.068	0.030
15	0.021	0.022	0.020	0.024	0.020	0.025	0.019	0.022	0.022	0.057	0.054	0.055	0.066	0.060	0.058	0.055	0.026
16	0.027	0.028	0.028	0.032	0.026	0.028	0.027	0.026	0.036	0.064	0.059	0.061	0.062	0.059	0.061	0.059	0.022
17	0.026	0.020	0.024	0.024	0.032	0.022	0.022	0.021	0.019	0.057	0.049	0.053	0.056	0.057	0.056	0.057	0.023
18	0.051	0.027	0.025	0.026	0.029	0.026	0.028	0.028	0.023	0.069	0.061	0.060	0.066	0.063	0.059	0.058	0.021
19	0.039	0.037	0.036	0.051	0.034	0.039	0.036	0.036	0.035	0.088	0.085	0.086	0.084	0.085	0.078	0.084	0.039
20	0.040	0.039	0.053	0.044	0.041	0.049	0.048	0.035	0.031	0.082	0.088	0.087	0.090	0.095	0.087	0.089	0.036
21	0.042	0.039	0.041	0.054	0.037	0.046	0.043	0.041	0.042	0.104	0.093	0.091	0.092	0.096	0.091	0.090	0.039
22	0.041	0.036	0.045	0.044	0.044	0.043	0.048	0.051	0.038	0.089	0.091	0.098	0.100	0.096	0.097	0.096	0.043
23	0.046	0.048	0.066	0.065	0.050	0.054	0.047	0.047	0.044	0.097	0.118	0.111	0.123	0.109	0.111	0.114	0.045
24	0.037	0.038	0.044	0.044	0.034	0.053	0.039	0.034	0.035	0.104	0.097	0.103	0.107	0.104	0.106	0.109	0.037
25	0.040	0.034	0.044	0.036	0.026	0.044	0.036	0.035	0.031	0.084	0.084	0.092	0.094	0.088	0.085	0.089	0.034
26	0.037	0.039	0.049	0.048	0.035	0.038	0.035	0.036	0.030	0.096	0.091	0.090	0.093	0.092	0.085	0.083	0.034
27	0.043	0.042	0.047	0.051	0.041	0.046	0.043	0.038	0.036	0.094	0.091	0.097	0.100	0.098	0.093	0.088	0.037
28	0.040	0.030	0.041	0.054	0.035	0.044	0.034	0.039	0.042	0.087	0.090	0.089	0.096	0.090	0.088	0.084	0.041
Probe	2.829	3.002	3.447	4.007*	3.360	3.529	3.292	3.399	3.322	11.614*	9.186	8.456	7.617	7.761	8.571	7.781	3.475

Data of sensor 8 and 10 not obtained due to sensor trouble
* Data including large noise components

JAXA Research and Development Report JAXA-RR-05-030E

Date of Issue: March 31, 2006
Edited and Published by: Japan Aerospace Exploration Agency
7-44-1 Jindaiji-higashimachi, Chofu-shi, Tokyo 182-8522, Japan
URL: http://www.jaxa.jp/
Printed by: TOKYO PRESS Co., Ltd.

Printed on Recycled Paper